International Journal of Solids and Structures 285 (2023) 112535

Contents lists available at ScienceDirect

International Journal of Solids and Structures

journal homepage: www.elsevier.com/locate/ijsolstr

Multi-scale modeling of shock wave propagation in energetic solid-state composites

Adam V. Duran [a], A. Ramazani [b,*], V. Sundararaghavan [a]

[a] Department of Aerospace Engineering, University of Michigan, Ann Arbor, MI 48109, USA
[b] Department of Mechanical Engineering, Massachusetts Institute of Technology, MA 02139, USA

ARTICLE INFO

Keywords:
Multi–scale Modeling
Shock Wave Propagation
Energetic solid state composites
Polymer-bonded explosives
Taylor–Galerkin finite element discretization

ABSTRACT

We present a novel structural dynamics code for modeling shock and detonation waves in Polymer-Bonded Explosives (PBXs), which are crucial for conventional munitions and propulsion components. Our code uses a stable and efficient solution strategy based on a Taylor–Galerkin finite element (FE) discretization to accurately predict PBX behavior under extreme shock loading. To model the PBXs, we implement equations of state for the solid unreacted material and gaseous reaction products using a pressure mixture rule governed by pressure-based reaction rates. We verify the FE model using analytical solutions for SOD shock and ZND detonation models. In addition to the continuum model, we also introduce a first-order multi-scale model that uses a Taylor approach to compute macro-scale fluxes and properties from the underlying microstructural sub-problems using averaging schemes. Our numerical results demonstrate the effectiveness of our multi-scale model in accurately predicting pressure profiles and detonation velocities for microstructures with varying mass fractions. These findings have significant implications for microstructure design and highlight the importance of considering microstructural variability in PBX behavior. Overall, our structural dynamics code represents a significant step towards improving the understanding and design of PBXs under extreme shock loading conditions.

1. Introduction

Energetic composite materials are widely utilized in applications such as propellants, explosives, and fuel cell components due to their rapid energy release, which involves complex nonlinear interactions between chemistry and mechanics. The detonation process involves sustaining a shock wave by the rapid release of chemical energy from the material, with extreme features such as speeds of several thousand meters per second and peak pressures of up to 100 GPa (Fickett and Davis, 1979). However, laboratory experiments are often insufficient to handle the safety and performance requirements of energetic composites, leading to significant interest in engineering these materials for specific shock sensitivity and energy output. Although decomposition and energy release occur at the molecular level, the transfer of chemical energy to thermal and mechanical energy occurs at larger scales, and material behavior is strongly influenced by the microstructure or material heterogeneities. Despite their significance in the literature, current Eulerian hydrocodes used to simulate PBX shock loading do not explicitly model these heterogeneities. For example, binder content has been shown to affect shock speed, and the strength and content of the matrix material affect the time to detonation (Dobratz and Crawford, 1985; Duan et al., 2010). In this study, we adopt a first-order multiscale modeling approach using a Taylor method to investigate the impact of increasing binder content on PBX detonation (Lee and Sundararaghavan, 2011). The macro-scale is represented by a homogenized continuum, with the macro-scale fields uniformly distributed to the micro-scale, as illustrated in Fig. 1. Macro-scale fluxes and properties are computed at all integration points using averaging schemes based on the underlying microstructural sub-problems.

The evolution of solid-state composites during detonation can be achieved by solving the reactive Euler equations, a set of nonlinear hyperbolic equations. However, traditional displacement-based formulations of solid dynamics are unsuitable due to locking issues at extreme mesh distortions and errors in wave propagation velocities. The fluid dynamics community has addressed this problem using Riemann solvers, primarily in the context of Eulerian finite volume methods (Menikoff, 2006; Baer, 2000; Baer and Trott, 2002; Benson and Conley, 1999; Brundage et al., 2009; Reaugh, 2006). Stabilized methods, such as Petrov–Galerkin (PG), Galerkin/least-squares (GLS), and Taylor–Galerkin (TG), have been developed to address the issue in the context of standard finite element methods. In PG and GLS methods, an artificial diffusion term with a semi-empirical coefficient is added to the weak form as a stabilization term. However, the coefficient

* Corresponding author.
E-mail addresses: ramazani@mit.edu (A. Ramazani), veeras@umich.edu (V. Sundararaghavan).

https://doi.org/10.1016/j.ijsolstr.2023.112535
Received 15 April 2023; Received in revised form 19 September 2023; Accepted 19 October 2023
Available online 27 October 2023

Nomenclature

U	State vector
F	Flux vector
S	Source vector
t	Time (μs)
x	Distance (cm)
A	Jacobian
ρ	Density (g/cm^3)
ρ_i	Density of species i (g/cm^3)
u	Velocity (cm/μs)
ρE	Energy per unit volume (Mbar)
λ	Burn fraction
λ_i	Burn fraction of species i
p	Pressure (Mbar)
$\overline{p}$	Average pressure (Mbar)
R	Reaction rate (μs^{-1})
M	Mass matrix
B	Force vector
Δt	Time step (μs)
d	Global smoothing parameter
χ	Local smoothing parameter
N_i	Mass fraction of species i
D	Detonation velocity (cm/μs)

choice may lead to overdamping (Raymond and Garder, 1976; Brooks and Hughes, 1982). The TG algorithm was originally proposed by Donea (Donea, 1984), Baker et al. Baker and Kim (1987), and Löhner et al. (1984) for first-order systems of hyperbolic equations, in which the Galerkin space discretization follows the Taylor expansion in time. TG finite element schemes have an advantage in that they do not have any free parameters, and the diffusion arises from an improved Taylor approximation to the time derivative of the fields. Although TG algorithms have been successfully applied in areas such as pollutant transport, shallow water problems, and fluid dynamics (Nassehi and Bikangaga, 1993; Quecedo and Pastor, 2002; Lohner et al., 1987), no prior study has investigated the technique for multiscale reactive Euler equations.

Reactive-burn models rely on various reaction-rate equations. Arrhenius models use reaction schemes that are fine-tuned to experimental and chemical data, such as heats of formation. The reaction kinetics of PBXs are typically characterized by three stages: (i) endothermic dissociation, (ii) formation of short-lived, reactive intermediates, and (iii) exothermic recombination. However, measuring the intermediate species is difficult, so a one-step form (Menikoff, 2006) is often used to approximate the reaction kinetics, although other schemes like three-step (McGuire and Tarver, 1981), four-step (Tarver and Tran, 2004), or multi-step reactions (Henson et al., 2009) have also been proposed. To ensure thermal and pressure equilibrium, these models require empirical parameters. The Ignition and Growth model (Lee and Tarver, 1980) is a pressure-dependent model developed to simulate the ignition of hotspots and the growth of reaction from hotspots into the surrounding explosive, and it is based on empirical parameters. This model requires pressure equilibrium for both the solid unreacted explosive and the reacted products. The JWL++ model (Souers et al., 2000) is a simplified version of the Ignition and Growth model, which utilizes a mixture rule for the total pressure and has been shown to be equivalent to enforcing pressure equilibrium.

Each reaction state requires an equation of state. Different equations of state (EOS) have been employed to represent explosives, including the Jones–Wilkins–Lee (JWL) form (Lee and Tarver, 1980), the Murnaghan form (Souers et al., 2000), and the Gruneisen form (Baer, 2000). The Gruneisen form has been used in various studies due to its linear shock velocity versus particle velocity Hugoniot (Baer, 2000; Conley et al., 1998; Menikoff and Kober, 2000). The JWL form is the most popular equation of state for gaseous reaction products, developed by measuring the expansion velocity of metal casings surrounding HMX (Kury et al., 1965). In this study, the Murnaghan equation of state represents the unreacted solid, while the C-form JWL equation of state represents the reacted detonation products. Section 2 outlines the governing equations, followed by the T–G algorithm in Section 3. The equations of state and continuum model are covered in Section 4, while Section 5 presents the multiscale model and its results, including a study of the effect of binder content distribution in the microstructure on measured shock speeds.

2. Governing equations

In order to understand the influence of microstructure on PBXs, it is critical to develop a reliable computational model at the meso-scale. The behavior of the material during detonation can be replicated through the solution of the reactive Euler equations. Although some two-dimensional simulations have been performed, we present the one-dimensional reactive Euler equations for ease of understanding. These equations are vector-based, containing partial derivatives denoted by subscripts "x" and "t", and do not incorporate radiation effects, viscosity, or diffusion.

$$U_t + F_x = S \tag{1}$$

with

$$U = \begin{Bmatrix} \rho \\ \rho u \\ \rho E \\ \rho \lambda \end{Bmatrix} \quad F = \begin{Bmatrix} \rho u \\ \rho u^2 + p \\ (\rho E + p)u \\ \rho u \lambda \end{Bmatrix} \quad S = \begin{Bmatrix} 0 \\ 0 \\ 0 \\ \rho R(p, \lambda) \end{Bmatrix} \tag{2}$$

The proportion of reactants and products in a material is measured by the burn fraction λ. The value of λ is 0 when the material is unreacted and 1 when it is completely reacted. The transport equation for the burn fraction includes the reaction rate term $R(p, \lambda)$, which depends on both the pressure and the burn fraction. The Ignition and Growth equation provides an expression for the reaction rate, as shown below. The relative volume η is defined as the ratio of the density ρ to the reference density ρ_0. The empirical parameters for this model are obtained from Ref. Lee and Tarver (1980) and are presented in Table 1. The reactive model is described by vector equations, which do not consider diffusion, viscosity, or radiation effects.

$$R(p, \lambda) = I(1 - \lambda)^{2/9}\eta^4 + G(1 - \lambda)^{2/9}\lambda^{2/3}p^z \tag{3}$$

3. Numerical scheme

3.1. One-step Taylor Galerkin scheme

The 1D reactive Euler equations given by Eq. (1) are solved using a one-step Taylor Galerkin scheme. This widely used time-stepping algorithm is second-order accurate, explicit and analogous to the Lax–Wendroff method. Taking a Taylor series expansion of U

$$U^{n+1} = U^n + \Delta t U_t^n + \frac{1}{2}\Delta t^2 U_{tt}^n + \mathcal{O}(\Delta t^3) \tag{4}$$

where t^{n+1} is the current time and t^n is the previous time. The first term of the RHS of Eq. (4) is the state vector U from Eq. (2). The second term is found from rearranging Eq. (1); i.e.

$$U_t = -F_x + S \tag{5}$$

The third term from the Taylor expansion is found by differentiating Eq. (5) with respect to time. The Euler equations are written in the

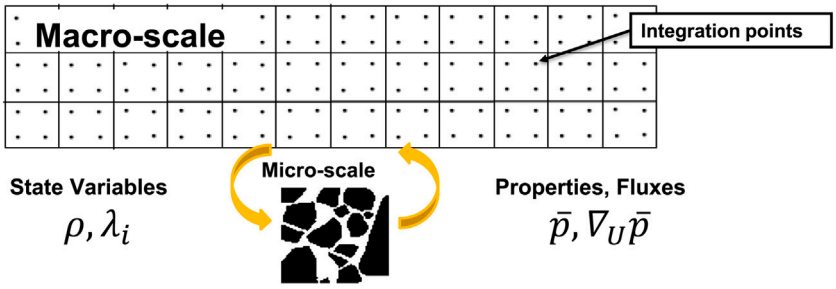

Fig. 1. Multiscale modeling approach.

Table 1
Constants.

Constant	PBX 9501 (Lee and Tarver, 1980) (Dobratz and Crawford, 1985) Value	HMX (Handley, 2011) Value	Binder (Handley, 2011) Value	Units
I	44	44	44	μs^{-1}
G	200	200	200	μs^{-1} $Mbar^{-z}$
z	1.6	1.6	1.6	
ρ_0	1.84	1.891	1.27	g/cm^3
a	0.267	0.2901	0.24	cm/μs
b	1.906	2.058	1.70	
A	8.520	7.717	2.0879	Mbar
B	0.1802	0.1064	0.0071	Mbar
C	0.01207	0.0085	0.0038	Mbar
R_1	4.55	4.2	4.33	
R_2	1.30	1.0	0.645	
ω	0.38	0.30	0.09	

quasi-linear form with Jacobian matrices $A = \partial F/\partial U$ and as a result flux vectors are rewritten as $F = AU$. Now Eq. (4) is expressed as

$$U^{n+1} = U^n + \Delta t(S - F_x)^n + \frac{1}{2}\Delta t^2[S_t - (AS - A^2U_x)_x]^n \tag{6}$$

The rate of the source term S_t is found by performing finite differences on S from Eq. (2); i.e. $S_t = (S^n - S^{n-1})/\Delta t$. The associated variational form is given as follows after integration by parts of the spatial terms

$$\begin{aligned}\int_0^L W\,\frac{U^{n+1}-U^n}{\Delta t}\,dx &= \int_0^L W\,S^n\,dx + \int_0^L W_x\,F^n\,dx + \frac{1}{2}\Delta t\int_0^L W\,S_t^n\,dx \\ &+ \frac{1}{2}\Delta t\int_0^L W_x(AS - A^2U_x)^n dx - \left[W\cdot(F^n + \frac{1}{2}\Delta t(AS - A^2U_x)^n)\right]_{x=0}^{x=L}\end{aligned} \tag{7}$$

Modifying the boundary term based on the relation $F_t^n = F_u U_t^n = A(S - F_x)^n = (AS - A^2U_x)^n$,

$$\begin{aligned}\int_0^L W\,\frac{U^{n+1}-U^n}{\Delta t}\,dx &= \int_0^L W\,S^n\,dx + \int_0^L W_x\,F^n\,dx + \frac{1}{2}\Delta t\int_0^L W\,S_t^n\,dx \\ &+ \frac{1}{2}\Delta t\int_0^L W_x(AS - A^2U_x)^n dx - \left[W\cdot(F^n + \frac{1}{2}\Delta t F_t^n)\right]_{x=0}^{x=L}\end{aligned} \tag{8}$$

In this work, flux representation depends on the compressibility. In regions of compression where $\partial u/\partial x < 0$ a group representation, shown in Eq. (9) is used, and the classical flux representation is used otherwise.

$$F = \sum_{k=1}^{2} W_k(x)F(U_k) \tag{9}$$

where k corresponds to the nodes of the elements.

3.2. Numerical treatment of shocks

To obtain non-oscillatory solutions in the presence of sharp gradients, a high-resolution scheme is used to handle shocks with minimal numerical dissipation. The scheme applies numerical dissipation only in the proximity of a discontinuity, where the diffusion coefficient is determined based on the local solution characteristics. After the Galerkin spatial discretization, the resulting algebraic equation can be expressed as follows:

$$M(U^{n+1} - U^n) = \Delta t B^n \tag{10}$$

The consistent mass matrix M acting on U^{n+1} is replaced by a diagonal matrix M^L obtained by row sum and a dissipation parameter (d) is added.

$$M^L(U^{smooth} - U^{n+1}) = d(M - M^L)U^{n+1} \tag{11}$$

Eqs. (10) and (11) represent a two stage procedure where the desired solution is U^{smooth}. For a value of $d > 0$ the system adds dissipation to the entire system; i.e. global smoothing. Local smoothing is produced by controlling d locally, in the presence of shocks. Locally, at a node "i" Eq. (11) is

$$M^L(U^{smooth} - U^{n+1}) = \sum_j d_{ij}M_{ij}(U_j^{n+1} - U_i^{n+1}) \tag{12}$$

where nodes "j" are connected to node "i" and dissipation (d_{ij}) is controlled locally in each nodal connection. To detect the presence of shocks d_{ij} is constructed by considering the pressure gradient (Donea and Huerta, 2003).

$$d_{ij} = min[\chi max(d_i, d_j), 1] \tag{13}$$

where χ is a free parameter and d_i and d_j are the local dissipation parameters at nodes i and j respectively. These local parameters activate at the presence of shocks. An effective shock sensor is constructed using pressure gradients

$$d_i = |\frac{pj - 2pi + pi\_}{pj + 2pi + pi\_}|,$$

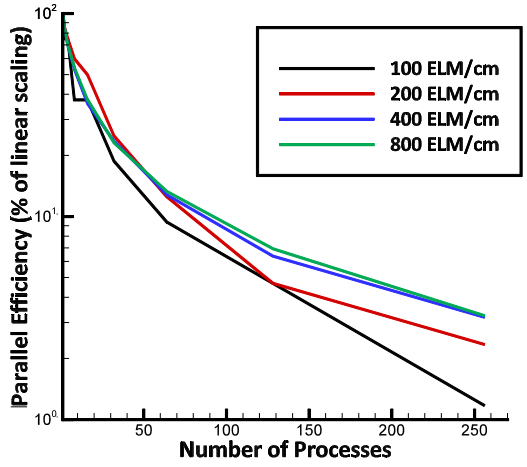

Fig. 2. The strong scaling efficiency (as a percentage of linear) versus number of processes for a 0.5 cm × 0.5 cm sample for a total of 10 time steps, Δt.

$$d_j = |\frac{pj_+ - 2pj + pi}{pj_+ + 2pj + pi}| \tag{14}$$

and

$$pi_- = pj - 2(xj - xi) \cdot [\nabla p]i,$$
$$pj_+ = pi - 2(xj - xi) \cdot [\nabla p]j. \tag{15}$$

where pj, and xj represent pressure and position of node j; and pi, and xi represent pressures and positions node i.

3.3. Computational implementation

The numerical scheme was written in the object-oriented programming language C++, which is often used for high performance computing(HPC) code development within scientific computing community due to its performance qualities. To aid in speeding up the solution process, the assembly process and solution scheme are parallelized. The solution requires sparse matrix inversion. The hydrocode was developed using the parallel toolbox PETSc and the solution of linear systems is accomplished using a GMRES solver along with block Jacobi and ILU preconditioning. The University of Michigan CAC's Flux cluster (27,000 cores-4 GB of RAM per core) was utilized for fast numerical implementation.

To test the computational performance of the solution process, scalability tests were performed. In general these tests examine the capability of solution process to an increase in data load or in resources. The solution procedure was ran for a 0.5 cm × 0.5 cm sample for a total of 10 time steps, Δt with results shown on Fig. 2. Strong scaling, defined by how the solution time varies with the number of processes for a fixed total problem size was preformed for various problem sizes. The strong scaling efficiency (as a percentage of linear) is given as by

$$100\left(\frac{t_1}{N\ t_N}\right) \tag{16}$$

where t_1 is the amount of time to complete a work unit with 1 process and t_N is the amount of time to complete the same unit of work with N processes. As expected, scaling efficiency decreases as the number of processes increases due to communication overhead; however, total computational time decreases. Increasing fidelity, or number of elements per centimeter, provides a higher scaling efficiency when the number of processes increases.

3.4. Numerical results for SOD shock and ZND

The developed numerical scheme is evaluated for stability and accuracy by applying it to the shock tube problem in classical fluid dynamics. This test involves two fluids with different pressures separated by a membrane. Upon removal of the membrane, a rarefaction wave, contact discontinuity, and shock wave are formed. The proposed scheme's numerical results are compared to the analytical solution for an ideal gas obtained using Riemann invariants, as shown in Figs. 3–5. The figures illustrate that the numerical results capture the distinct features of the test and agree well with the exact solution. To further verify the numerical scheme's accuracy for reactive flow, it is tested on the ZND detonation model, which produces a von Neumann spike propagating at a constant speed. As demonstrated in Figs. 6 and 7, the numerical results are compared to the exact solution and found to be in good agreement. A local smoothing parameter of $\chi = 3.0$ is used to obtain these results.

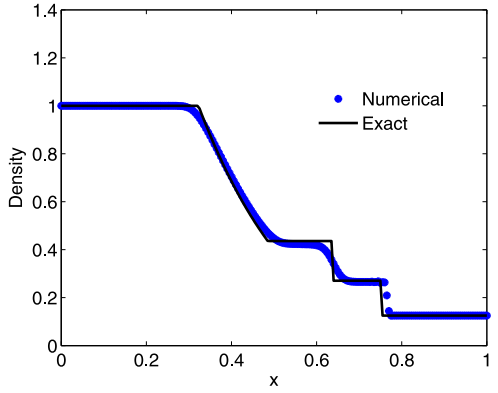

Fig. 3. SOD Shock tube density.

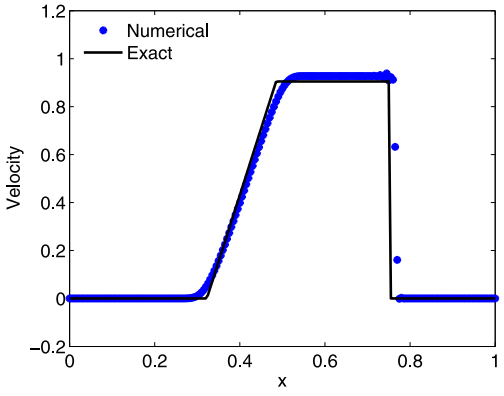

Fig. 4. SOD Shock tube velocity.

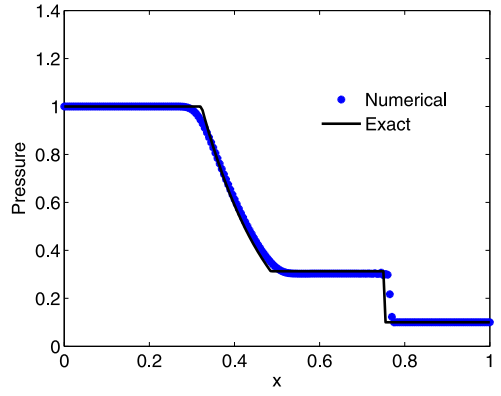

Fig. 5. SOD Shock tube pressure.

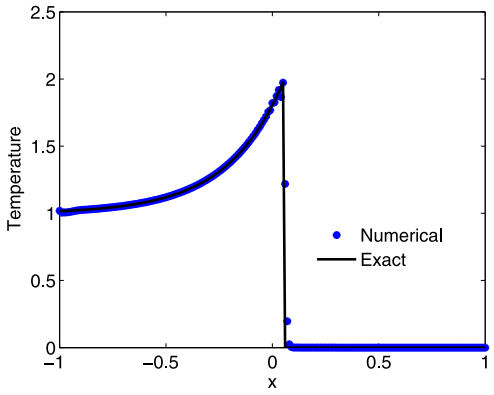

Fig. 6. ZND temperature.

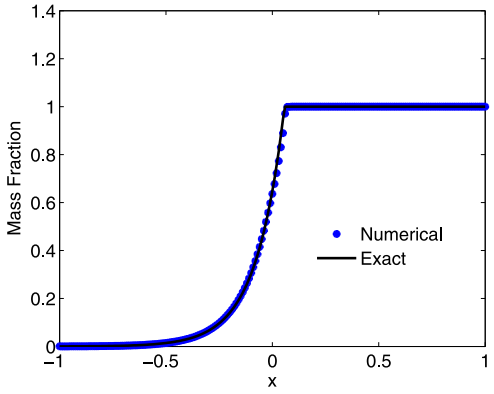

Fig. 7. ZND mass fraction.

4. Continuum model of polymer-bonded explosives

In the continuum model, it is considered a single component that represents the HMX and binder microstructure, with EOS parameters obtained from PBX 9501 experiments. To model both the pressure of unreacted material and reaction products of PBXs, it is necessary to represent the material when λ is neither 0 nor 1. In this work, we employ the JWL++ model, with subscripts "s" and "g" denoting solid and gas, respectively. For the unreacted equation of state, we use the Murnaghan equation, given by:

$$p = p_s = \frac{1}{n\kappa}\left(\frac{1}{(\rho_0/\rho)^n} - 1\right) \tag{17}$$

The values of n and κ are determined by fitting the linear shock relationship between the shock velocity U_S and the particle velocity u_p, based on the Hugoniot data available for several explosives. For the equation of state (EOS) of the fully reacted detonation products, a JWL in the C-term form is used. The EOS parameters for PBX 9501 are obtained from experiments detailed in Ref. Dobratz and Crawford (1985) and are listed in Table 1.

$$p = p_g = Ae^{-R_1\rho_0/\rho} + Be^{-R_2\rho_0/\rho} + \frac{C}{(\rho_0/\rho)^{1+\omega}} \tag{18}$$

For the intermediate state, a pressure mixture rule is used to find the total pressure.

$$p = (1-\lambda)p_s + \lambda p_g \tag{19}$$

Eq. (3) governs the burn fraction λ. In order to initiate a detonation wave in PBX 9501, the Hugoniot for the solid with $\lambda = 0$ and the reaction products with $\lambda = 1$ are computed as shown in Fig. 8. According to thermodynamics theory, the material must be shocked to

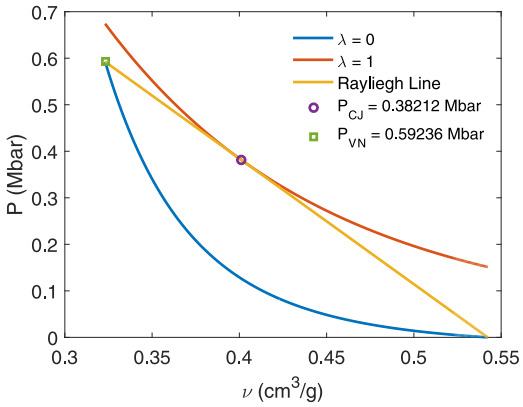

Fig. 8. Hugoniot for PBX 9501.

the Von Neumann pressure p_{VN} for the wave to be self-sustaining. The pressure then drops down the Rayleigh-line to the Chapman–Jouguet pressure p_{CJ}, which is the point of tangency with the Hugoniot of the reaction products. The Von Neumann pressure was determined by finding the intersection of the solid Hugoniot and the Rayleigh-line.

For the detonation simulation of PBX 9501, a numerical scheme described in the previous sections is used. The left side of the domain is pressurized to the calculated Von Neumann pressure $p_{VN} = 0.592$ Mbar, while the right side is left at ambient conditions with zero pressure. A uniform mesh of 1500 linear elements is used for a domain of 1.5 cm. The simulation is run for a duration of $t = 1$ μs with time-steps of $\Delta t = 1e^{-4}$ μs. Results for density, velocity, burn fraction, and pressure vs. distance are presented in Figs. 9–12 for time-steps of 0.2 μs. All solutions exhibit a stable, self-sustaining shock wave propagating through the domain. Initially, the density drops from the Von Neumann specific volume, and this region begins to expand below the reference density value. The velocity starts from zero and increases to peak values of around 3.5 km/s. The burn fraction λ is initially set to a pure solid, and as time progresses, the solid is burnt and completely reacted. There is a noticeable time disparity between the rate of reaction and shock speed. The pressure initially increases from the Von Neumann pressure p_{VN}. As the reaction initiates, the pressure recovers to p_{VN}, and a self-sustaining detonation progresses through the domain. The global smoothing parameter d is tuned to capture the peak Von Neumann point. For $d = 0.4$, the numerical peak of the pressure profile is $p = 0.574$ Mbar, which is a 3% difference from the calculated Von Neumann pressure. The same experiment for shocked PBX 9501 is performed in two dimensions. A radially symmetric detonation wave is used, with the initial discontinuity located at $r = 0.25$ cm. The combustion front is a quarter circle that expands as the system evolves. A uniform mesh with 150×150 quadrilateral elements is used with time-steps of $\Delta t = 5e^{-4}$ μs and no-slip boundary conditions. Numerical results at $t = 1$ μs for density, velocity, mass fraction, and pressure are shown in Figs. 13–16. The detonation profile maintains a symmetric circular shape through the experiment and is in good agreement with the 1D case.

5. First-order multiscale modeling of polymer-bonded explosives

In this section, we utilize a microstructure model that differentiates between HMX and binder components (in contrast to the continuum model in Section 4). To incorporate material heterogeneities, we employ first-order multiscale modeling via a Taylor approach. In this approach, we consider the volume fractions of HMX and binder components without enforcing equilibrium (see Ref. Lee and Sundararaghavan (2011)), providing an efficient way to account for micro-effects. The macro-scale is associated with a homogenized continuum, as shown in Fig. 1, with macro-scale fields passed uniformly to the micro-scale.

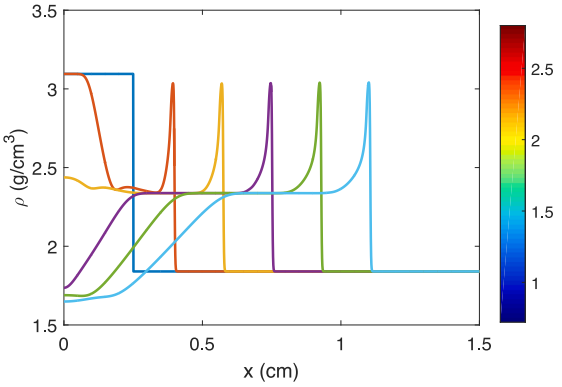

Fig. 9. Density for PBX 9501.

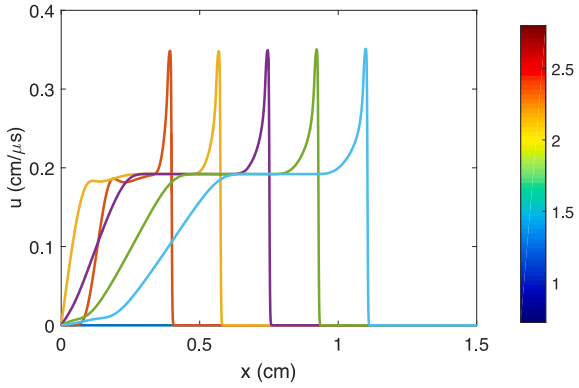

Fig. 10. Velocity for PBX 9501.

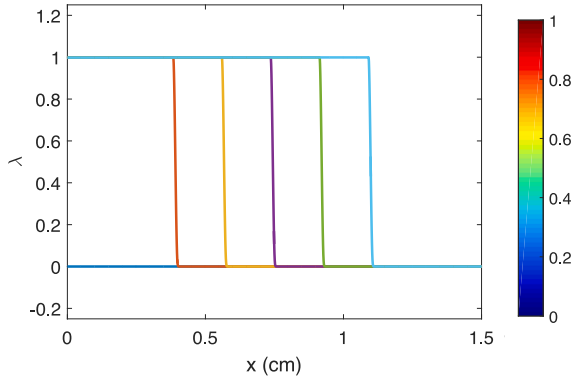

Fig. 11. Burn frac. for PBX 9501.

Macro-scale fluxes and properties are computed from the underlying microstructural sub-problems using averaging schemes at all integration points. To include variables for HMX and polymeric binder, denoted by subscripts H and B respectively, and an over-lined pressure ($\overline{p}$) indicating the averaged pressure in the microstructure, the 1D reactive Euler (macro) equations are updated.

$$U = \begin{Bmatrix} \rho \\ \rho u \\ \rho E \\ \rho_H \lambda_H \\ \rho_B \lambda_B \end{Bmatrix} \quad F = \begin{Bmatrix} \rho u \\ \rho u^2 + \overline{p} \\ (\rho E + \overline{p})u \\ \rho_H u \lambda_H \\ \rho_B u \lambda_B \end{Bmatrix} \quad S = \begin{Bmatrix} 0 \\ 0 \\ 0 \\ \rho_H R_H \\ \rho_B R_B \end{Bmatrix} \tag{20}$$

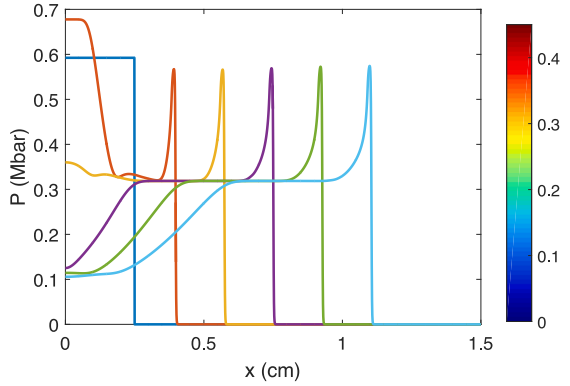

Fig. 12. Pressure for PBX 9501.

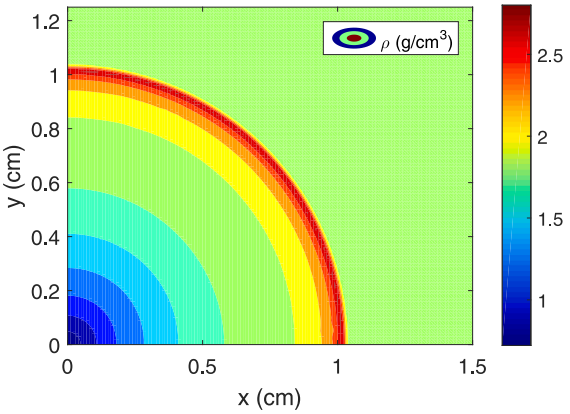

Fig. 13. Density for PBX 9501.

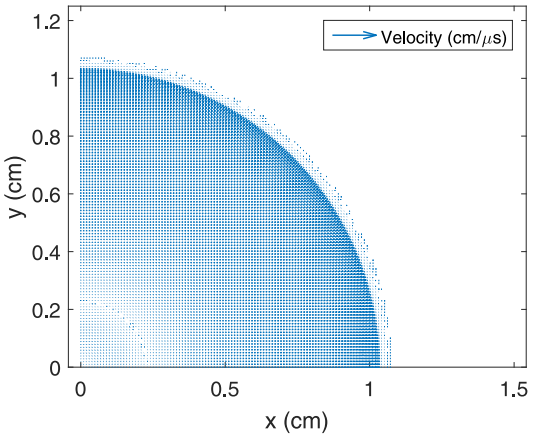

Fig. 14. Velocity for PBX 9501.

The total density is comprised of both HMX ρ_H and binder ρ_B and is split according to species mass fraction as indicated in Eq. (21).

$$\rho = \rho N_H + \rho N_B = \rho_H + \rho_B \tag{21}$$

The transport equation for burn fractions $\lambda_{H,B}$, are governed by the source term modeling the reaction rate $R_{H,B}(\rho_{H,B}, \lambda_{H,B})$. For a solid unreacted material $\lambda_{H,B} = 0$ and for the completely reacted products $\lambda_{H,B} = 1$. Burn fractions for both HMX and binder are governed by the previous Ignition and Growth model (Eq. (3)) with updated pressure

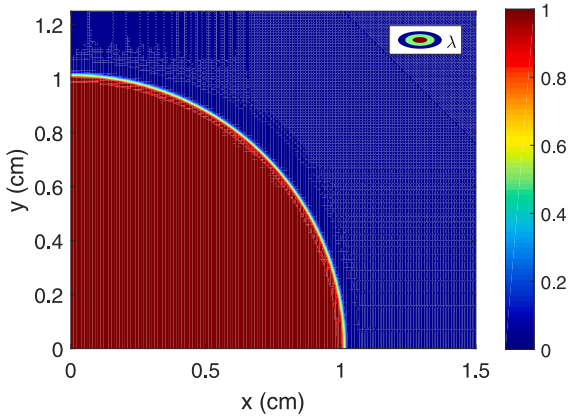

Fig. 15. Mass frac. for PBX 9501.

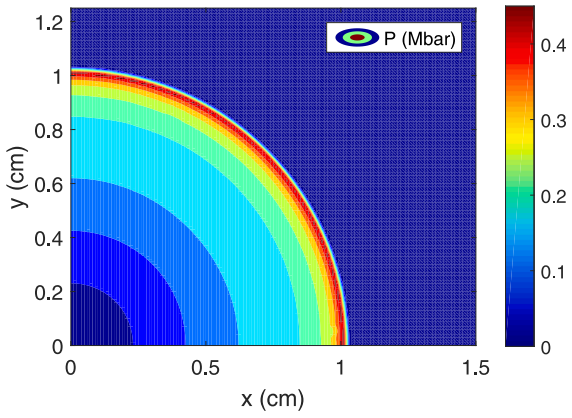

Fig. 16. Pressure for PBX 9501.

and burn fractions as follows.

$$R_{H,B}(p_{H,B}, \lambda_{H,B}) = I(1-\lambda_{H,B})^{2/9}\eta^4 + G(1-\lambda_{H,B})^{2/9}\lambda_{H,B}^{2/3}p_{H,B}^z \tag{22}$$

The average pressure of the composite, denoted by $\overline{p}$, is determined by calculating the pressures for both HMX and binder, using the JWL++ model (Souers et al., 2000). The Murnaghan equation, given by Eq. (17), is used as the unreacted equation of state for both HMX and binder ($p_{S(H,B)}$). The EOS of the fully reacted detonation products for both HMX and binder ($p_{G(H,B)}$) is modeled using a JWL in the C-term form, given by Eq. (18). The parameters for HMX and binder are obtained from Ref. Handley (2011) and are shown in Table 1. For the intermediate state, a pressure mixture rule is used to find the total pressure.

$$p_{H,B} = (1-\lambda_{H,B})p_{S,(H,B)} + \lambda_{H,B}p_{G,(H,B)} \tag{23}$$

Densities of HMX and binder calculated from Eq. (21) are passed to the equations of state (Eq. (17),(18)) and the total pressures for both HMX p_H and binder p_B are calculated from Eq. (23). The average pressure of the composite is calculated by the following equation and is based on the volume average of the calculated total pressures. This methodology is described graphically on Fig. 17.

$$\overline{p} = \frac{1}{V}\int p_i dV, \quad i = H, B \tag{24}$$

5.1. Numerical results for constant mass fraction

The comparison between the first-order multiscale model and the continuum model described in Section 4 is presented. The continuum model employs a homogeneous medium while the multiscale model takes material heterogeneity into consideration. Figs. 18 and 19 show a comparison of the Hugonoit and Rayleigh lines of the multiscale model (red curves) and the continuum model (black curves). By accounting for the microstructure of PBX 9501, the Hugonoit curve shifts, resulting in a reduction of the Von Neumann pressure from $p_{VN} = 0.592$ Mbar to $p_{VN} = 0.552$ Mbar, which corresponds to a difference of 7.25%. The detonation velocity for each model is determined using the relation between mass flow rate and the slope of the Rayleigh line, as illustrated in Fig. 19. The continuum model has a detonation velocity of $D = 0.892$ cm/μs, while the multiscale model has a detonation velocity of $D = 0.905$ cm/μs. The higher detonation velocity in the multiscale model is attributed to the explicit consideration of HMX content. Both models are initiated with their corresponding Von Neumann points, and numerical results for pressure and detonation wave speed are shown on Figs. 20 and 21, respectively. The pressures are directly compared at $t = 1$ μs on Fig. 20. The multiscale model's detonation wave travels faster than the continuum model's wave speed, as expected from the Rayleigh calculation. This is further supported by the detonation wave speeds indicated on Fig. 21. The detonation velocity is calculated by taking the mean value of shock speed over the final 0.6 μs of the simulation. The detonation velocities for the continuum model and multiscale model are $D = 0.881$ cm/μs and $D = 0.892$ cm/μs, respectively, with error bars indicating one standard deviation. These values are compared with the experimental detonation velocities (Dobratz and Crawford, 1985) for PBX 9501 and HMX on Fig. 21. Both detonation velocities fall within the experimental range, with pure HMX acting as the upper bound and PBX 9501 acting as the lower bound. The homogenized continuum approach leads to a slower shock speed, similar to that of PBX 9501, while the multiscale method approaches the velocity of pure HMX.

5.2. Numerical results for variable mass fraction

As the multiscale model considers both HMX and binder, we examine how variability in binder content affects shock speeds. All cases have an average binder content similar to that of PBX 9501 (5%) but with heterogeneity across the domain. Fig. 22 depicts a linear increase, a linear decrease, a parabolic increase, and a random distribution for HMX mass fractions ranging from $0.85 < N_H < 1$. The sample is subjected to a shock at $p_{VN} = 0.552$ Mbar, which is the Von Neumann pressure calculated for the constant mass fraction experiment, with the same time step, mesh size, and smoothing parameter. Peak pressures and detonation velocities for each sample are shown on Figs. 23 and 24, respectively, with error bars indicating one standard deviation. Peak pressure for each sample was obtained by taking a time average over the final 0.6 μs of the simulation. The peak pressure remains relatively uniform ($\overline{p} = 0.53$) across samples, with the highest average observed for the parabolic distribution, as illustrated in Fig. 24. The small standard deviations indicate a stable peak pressure during detonation. The detonation velocity was calculated by taking the mean value of the shock speed over the final 0.6 μs of the simulation. The detonation velocity between the constant mass fraction sample and the linearly decreasing sample remains relatively constant as both samples are dominated by HMX during the ignition phase of the reaction. However, when compared to the linearly increasing sample, the detonation velocity is lower. The parabolic sample has a much higher detonation velocity and peak pressure than other samples, as it contains a larger area of HMX-dominated regions. For the parabolic distribution, the largest uniform area, located at the center of the domain, has a mass fraction of $N_H = 0.99$, as shown in Fig. 22. All mean detonation velocities, except for the random sample, fall within the experimental bounds. However, the standard deviation shows a wide range of detonation velocities, including some within the bounds. Overall, we found that a parabolic distribution yields the best shock speeds, with implications for microstructure design.

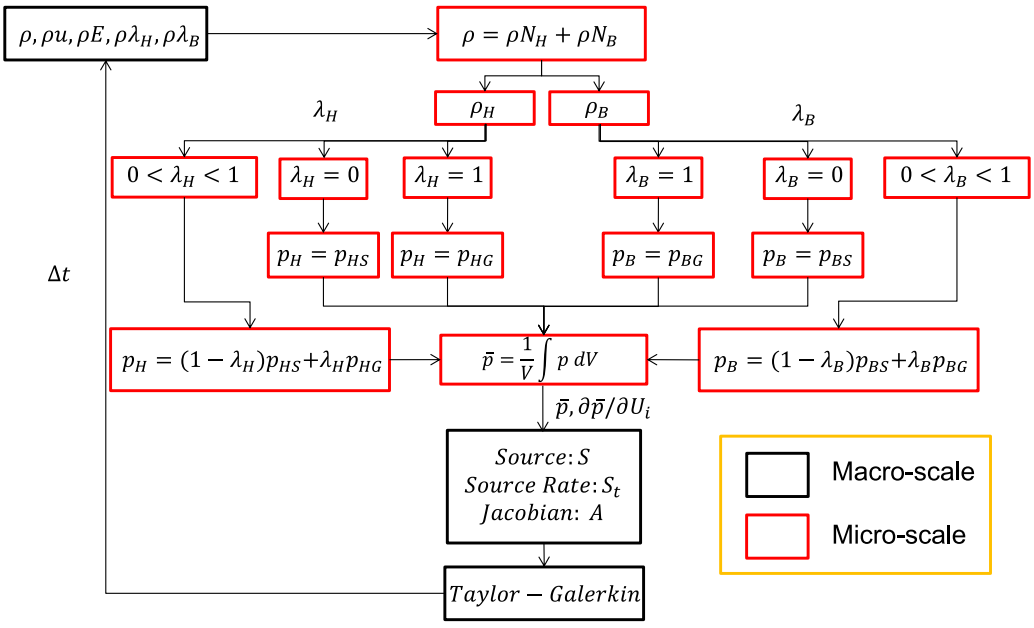

Fig. 17. Multiscale modeling methodology.

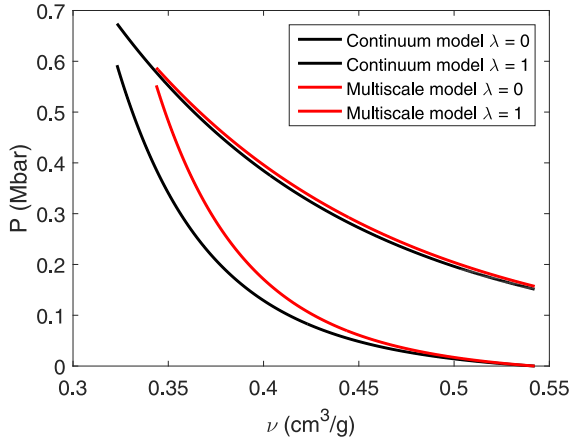

Fig. 18. Hugonoit for continuum and multiscale model.

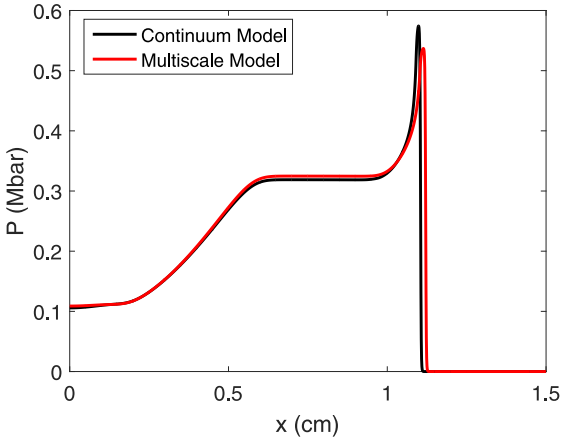

Fig. 20. Pressure profile for continuum and multiscale model.

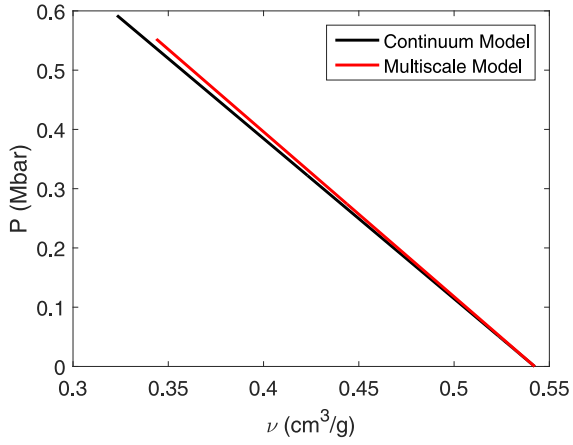

Fig. 19. Rayleigh line for continuum and multiscale model.

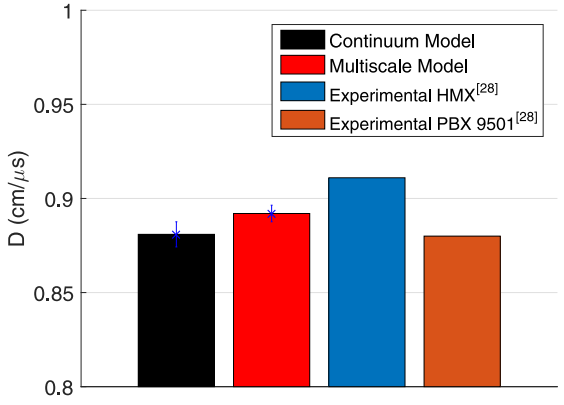

Fig. 21. Shock speed for continuum and multiscale model.

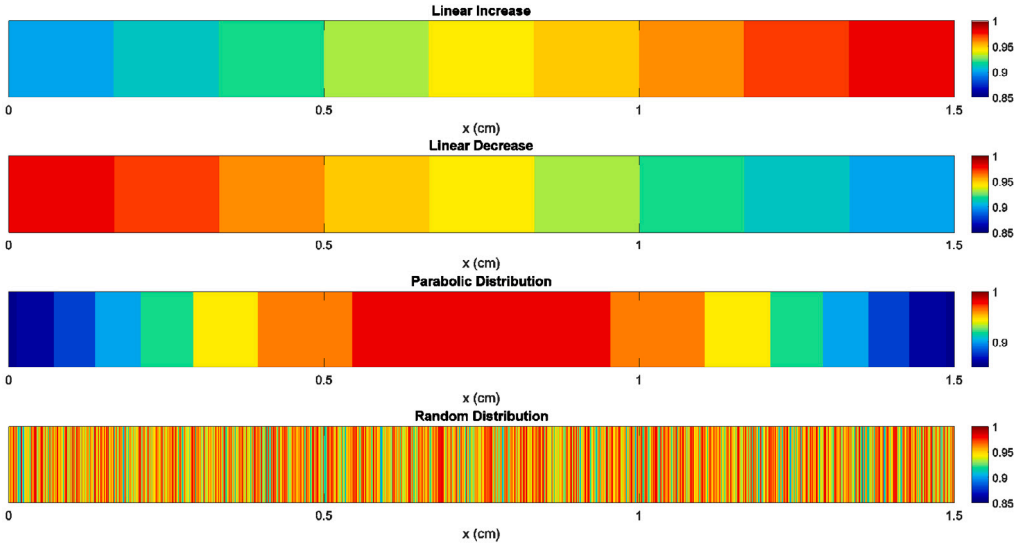

Fig. 22. Linear increase, linear decrease, a parabolic and random distribution for N_H (top to bottom).

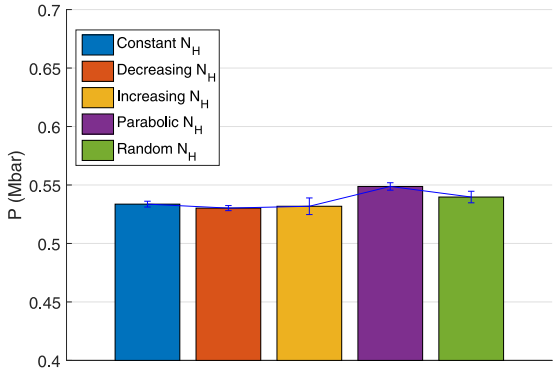

Fig. 23. Peak $\bar{p}$ for varying N_H.

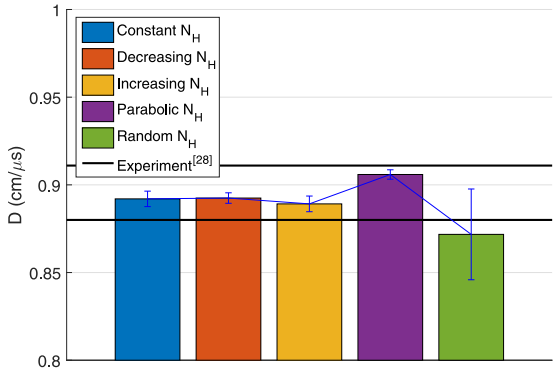

Fig. 24. Shock speed for varying N_H.

6. Conclusion

A direct numerical simulation has been carried out to study the propagation of shocks through PBXs using a one-step second-order Taylor–Galerkin scheme. We tested the scheme by comparing its results with exact solutions for the SOD shock tube problem and the ZND detonation model. To model the PBX, we used a pressure-based reaction scheme based on the Ignition and Growth model and the Murnaghan and JWL equations of state for unreacted solid and fully reacted product, respectively. The total pressure was determined using an analytic mixture rule. Our numerical detonation experiments of PBX 9501 demonstrated self-sustaining shock wave fronts traveling through the sample. We adjusted the global damping parameter to tune the numerical peak pressure and obtained good agreement with the Von Neumann pressure calculated from the Hugonoit. In addition, we presented initial work on multiscale modeling using a Taylor approach that explicitly modeled HMX and binder properties in PBX 9501. We showed that modeling the microstructure led to differences in pressure wave profiles and detonation wave speeds. We compared samples with varying mass fractions and found that microstructural variability had an impact on shock speeds. A parabolic distribution resulted in higher wave speeds and was deemed optimal for microstructure design, which has important implications. Future work will include full-order modeling where microstructural equilibrium is explicitly accounted for.

Declaration of competing interest

The authors declare the following financial interests/personal relationships which may be considered as potential competing interests: Veera Sundararaghavan reports a relationship with National Science Foundation that includes: funding grants. Veera Sundararaghavan reports a relationship with Defense Threat Reduction Agency that includes: funding grants.

Data availability

Data will be made available on request.

Acknowledgments

This material is based upon work supported by the National Science Foundation Graduate Research Fellowship Program Under DGE 1256260 and The Defense Threat Reduction Agency under HDTRA1-13-1-0009.

References

Baer, M.R., 2000. Computational modeling of heterogeneous reactive materials at the mesoscale. Shock Compress. Condens. Matter 505 (1), 27–34.

Baer, M.R., Trott, W.M., 2002. Theoretical and experimental mesoscale studies of impact-loaded granular explosive and simulant materials. In: Twelfth International Detonation Symposium.

Baker, A.J., Kim, J.W., 1987. A taylor weak statement algorithm for hyperbolic conservation laws. Internat. J. Numer. Methods Fluids 7 (5), 489–520.
Benson, D.J., Conley, P., 1999. Eulerian finite-element simulations of experimentally ecquired HMX microstructures. Modelling Simul. Mater. Sci. Eng. 7 (3), 333.
Brooks, A.N., Hughes, T.J., 1982. Streamline upwind/Petrov–Galerkin formulations for convection dominated flows with particular emphasis on the incompressible Navier–Stokes equations. Comput. Methods Appl. Mech. Engrg. 32 (1), 199–259.
Brundage, A.L., Wixom, R.R., Tappan, A.S., Long, G.T., 2009. Mesoscale simulations of shock initiation in energetic materials characterized by three-dimensional nanotomography. In: Proceedings of the American Physical Society Topical Group on Shock Compression of Condensed Matter, Vol. 1195, No. 1. AIP Publishing, pp. 315–318.
Conley, P.A., Benson, D.J., Howe, P.M., 1998. Microstructural effects in shock initiation. In: Eleventh International Detonation Symposium, ONR33300. pp. 768–780.
Dobratz, B.M., Crawford, P.C., 1985. LLNL Explosives Handbook: Properties of Chemical Explosives and Explosive Simulants. University of California URCL-52997.
Donea, J., 1984. A taylor Galerkin method for convective transport problems. Internat. J. Numer. Methods Engrg. 20 (1), 101–119.
Donea, J., Huerta, A., 2003. Finite Element Methods for Flow Problems. John Wiley and Sons.
Duan, Z.P., Wen, L.J., Liu, Y., Ou, Z.C., Huang, F.L., Zhang, Z.Y., 2010. A pore collapse model for hot-spot ignition in shocked multi-component explosives. Int. J. Nonlinear Sci. Numer. Simul. 11 (Supplement), 19–24.
Fickett, W., Davis, W.C., 1979. Detonation. Berkeley.
Handley, C.A., 2011. Numerical Modelling of Two HMX-Based Plastic-Bonded Explosives At the Mesoscale (Ph.D. thesis). University of St. Andrews UK.
Henson, B.F., Smilowitz, L., Romero, J.J., Asay, B.W., 2009. Modeling thermal ignition and the initial conditions for internal burning in PBX 9501. In: Proceedings of the American Physical Society Topical Group on Shock Compression of Condensed Matter, Vol. 1195, No. 1. pp. 257–262.
Kury, J.W., Hornig, H.C., Lee, E.L., McDonnel, J.L., Ornellas, D.L., Finger, M., Wilkins, M.L., 1965. Metal acceleration by chemical explosives. In: Fourth (International) Symposium on Detonation, ACR-126.
Lee, S., Sundararaghavan, V., 2011. Multi–scale modeling of moving interface problems with flux and field jumps: Application to oxidative degradation of ceramic matrix composites. Internat. J. Numer. Methods Engrg. 85 (6), 784–804.
Lee, E.L., Tarver, C.M., 1980. Phenomenological model of shock initiation in heterogeneous explosives. Phys. Fluids 23 (12), 2362–2372.
Lohner, R., Morgan, K., Peraire, J., Vahdati, M., 1987. Finite element flux corrected transport (FEM-FCT) for the Euler and Navier Stokes equations. Internat. J. Numer. Methods Fluids 7 (10), 1093–1109.
Löhner, R., Morgan, K., Zienkiewicz, O.C., 1984. The solution of nonlinear hyperbolic equation systems by the finite element method. Internat. J. Numer. Methods Fluids 4 (11), 1043–1063.
McGuire, R.R., Tarver, C.M., 1981. Chemical Decomposition Model for the Thermal Explosion of Confined HMX, RDX and TNT Explosives. Lawrence Livermore National Lab, CA (USA).
Menikoff, R., 2006. Detonation waves in PBX 9501. Combust. Theory Model. 10 (6), 1003–1021.
Menikoff, R., Kober, E., 2000. Compaction waves in granular HMX. Shock Compress. Condens. Matter 505 (1), 397–400.
Nassehi, V., Bikangaga, J.H., 1993. A mathematical model for the hydrodynamics and pollutants transport in long and narrow tidal rivers. Appl. Math. Model. 17 (8), 415–422.
Quecedo, M., Pastor, M., 2002. A reappraisal of taylor Galerkin algorithm for Drying Wetting Areas in shallow water computations. Internat. J. Numer. Methods Fluids 38 (6), 515–531.
Raymond, W.H., Garder, A., 1976. Selective damping in a Galerkin method for solving wave problems with variable grids. Mon. Weather Rev. 104 (12), 1583–1590.
Reaugh, J.E., 2006. Multi-Scale Computer Simulations To Study the Reaction Zone of Solid Explosives. United States Department of Energy.
Souers, P.C., Anderson, S., Mercer, J., McGuire, E., Vitello, P., 2000. JWL++: A simple reactive flow code package for detonation. Propell. Explosives, Pyrotechnics 25 (2), 54–58.
Tarver, C.M., Tran, T.D., 2004. Thermal decomposition models for HMX-based plastic bonded explosives. Combust. Flame 137 (1), 50–62.